# Exposing the inadequacy of redox formalisms by resolving redox inequivalence within isovalent clusters

Amymarie K. Bartholomew[a,1,2], Justin J. Teesdale[a,1], Raúl Hernández Sánchez[a,3], Brian J. Malbrecht[a], Cristin E. Juda[a], Gabriel Ménard[a,4], Wei Bu[b], Diana A. Iovan[a,5], Alexandre A. Mikhailine[a], Shao-Liang Zheng[a], Ritimukta Sarangi[c], SuYin Grass Wang[b], Yu-Sheng Chen[b], and Theodore A. Betley[a,6]

[a]Department of Chemistry and Chemical Biology, Harvard University, Cambridge, MA 02138; [b]ChemMatCARS, The University of Chicago, Argonne, IL 60439; and [c]Stanford Synchrotron Radiation Lightsource, SLAC National Accelerator Laboratory, Stanford University, Menlo Park, CA 94025-07015

Edited by Edward I. Solomon, Stanford University, Stanford, CA, and approved June 25, 2019 (received for review May 3, 2019)

**In this report we examine a family of trinuclear iron complexes by multiple-wavelength, anomalous diffraction (MAD) to explore the redox load distribution within cluster materials by the free refinement of atomic scattering factors. Several effects were explored that can impact atomic scattering factors within clusters, including 1) metal atom primary coordination sphere, 2) M–M bonding, and 3) redox delocalization in formally mixed-valent species. Complexes were investigated which vary from highly symmetric to fully asymmetric by $^{57}$Fe Mössbauer and X-ray diffraction to explore the relationship between MAD-derived data and the data available from these widely used characterization techniques. The compounds examined include the all-ferrous clusters [$^{n}$Bu$_4$N][($^{tbs}$L)Fe$_3$($\mu^3$–Cl)] (1) ([$^{tbs}$L]$^{6-}$ = [1,3,5-C$_6$H$_9$(NC$_6$H$_4$-*o*-NSi$^{t}$BuMe$_2$)$_3$]$^{6-}$]), ($^{tbs}$L)Fe$_3$(py) (2), [K(C$_{222}$)]$_2$[($^{tbs}$L)Fe$_3$($\mu^3$–NPh)] (4) (C$_{222}$ = 2,2,2-cryptand), and the mixed-valent ($^{tbs}$L)Fe$_3$($\mu^3$–NPh) (3). Redox delocalization in mixed-valent 3 was explored with cyclic voltammetry (CV), zero-field $^{57}$Fe Mössbauer, near-infrared (NIR) spectroscopy, and X-ray crystallography techniques. We find that the MAD results show an excellent correspondence to $^{57}$Fe Mössbauer data; yet also can distinguish between subtle changes in local coordination geometries where Mössbauer cannot. Differences within aggregate oxidation levels are evident by systematic shifts of scattering factor envelopes to increasingly higher energies. However, distinguishing local oxidation levels in iso- or mixed-valent materials can be dramatically obscured by the degree of covalent intracore bonding. MAD-derived atomic scattering factor data emphasize in-edge features that are often difficult to analyze by X-ray absorption near edge spectroscopy (XANES). Thus, relative oxidation levels within the cluster were most reliably ascertained from comparing the entire envelope of the atomic scattering factor data.**

redox distribution | clusters | bioinorganic

Traditional coordination complexes mediate redox processes from discrete orbitals (1–3). The electroactive orbitals need not be uniquely metal-based and may include both transition metal and ligand character (4–11). For extended solids, local coordination environments change for surface-bound elements, but the redox load is distributed within the valence band under oxidative stress, or the conduction band under reducing conditions. Clusters represent the intermediate domain as they contain M–M bonding interactions at the core and are terminated by metal–ligand interactions at the periphery (12). Clusters maintain the properties of mononuclear coordination compounds in that redox still occurs in discrete orbitals, yet begin to approximate band-like configurations as the cluster size increases, increasing the density of near-degenerate orbitals. A variety of analytical techniques (e.g., near-infrared spectroscopy, cyclic voltammetry, $^{57}$Fe Mössbauer) can be used to interrogate delocalization. However, these bulk techniques cannot provide site-specific information with regard to redox load on the individual metals within a cluster. Understanding how redox loads are distributed within clusters can provide important details about the mechanisms of substrate activation and redox changes both in biological and abiological systems.

Multiwavelength anomalous X-ray diffraction (MAD) has the potential to be a powerful technique for understanding the local oxidation state of transition metals in both synthetic clusters and polynuclear biological cofactors. In theory, MAD can serve as a site-specific, crystallographic probe of a metal center's absorption edge profile, analogous to employing X-ray absorption near edge spectroscopy (XANES) in mononuclear compounds. However, examples of its application to molecular and biological systems are thus far limited. As the capacity to collect well-resolved MAD spectra improves, it is necessary to benchmark the results of MAD on polynuclear clusters. The effects of fully delocalized mixed valency and changes in local bond metrics and M–M separation must be investigated as these factors affect the appearance of MAD data in ways that can impact the

## Significance

**Identifying the redox states within polynuclear cofactors in biology is critical for elucidating substrate binding sites. Multiple-wavelength, anomalous X-ray diffraction (MAD) has been used to address the redox states within the polynuclear cofactors in nitrogenase. While MAD provides a site-specific analytical technique to resolve differences in relative redox states within molecular species, we note that rigorous application of this technique on well-defined synthetic iso- and mixed-valent clusters has not been performed. Our report illustrates the large variation observed for nominally isovalent sites, thus providing a much-needed calibration on what to expect for resolving redox load distribution within cluster materials.**

Author contributions: A.K.B., J.J.T., R.H.S., B.J.M., and T.A.B. designed research; A.K.B., J.J.T., R.H.S., B.J.M., C.E.J., G.M., W.B., D.A.I., A.A.M., R.S., S.G.W., and Y.-S.C. performed research; A.K.B., J.J.T., R.H.S., C.E.J., and G.M. contributed new reagents/analytic tools; A.K.B., J.J.T., R.H.S., B.J.M., S.-L.Z., and T.A.B. analyzed data; and A.K.B., J.J.T., R.H.S., and T.A.B. wrote the paper.

The authors declare no conflict of interest.

This article is a PNAS Direct Submission.



Data deposition: The atomic coordinates and structure factors have been deposited in the Cambridge Crystallographic Data Centre (accession nos. 1897925–1897928).

[1]A.K.B. and J.J.T. contributed equally to this work.

[2]Present address: Department of Chemistry, Columbia University, New York, NY 10027.

[3]Present address: Department of Chemistry, University of Pittsburgh, Pittsburgh, PA 15260.

[4]Present address: Chemistry and Biochemistry, University of California, Santa Barbara, CA 93106.

[5]Present address: Department of Chemistry, University of California, Berkeley, CA 94720.

[6]To whom correspondence may be addressed. Email: betley@chemistry.harvard.edu.

This article contains supporting information online at www.pnas.org/lookup/suppl/doi:10.1073/pnas.1907699116/-/DCSupplemental.

Published online July 19, 2019.

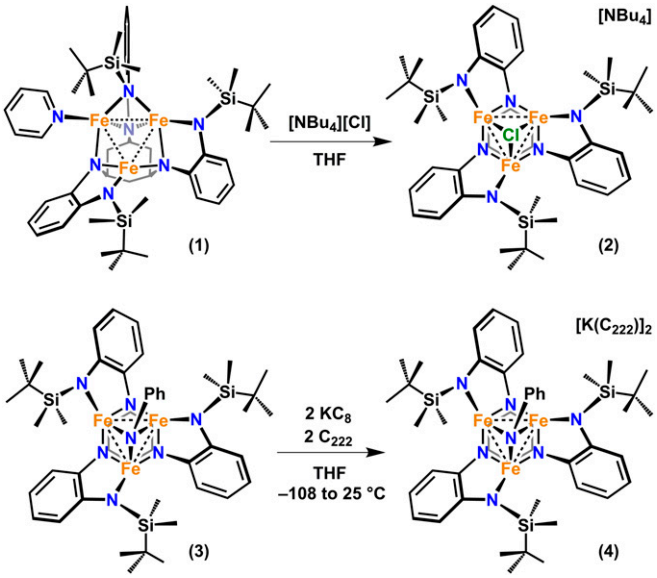


**Fig. 1.** Synthesis of **1**–**4**.

interpretation of MAD as it is applied to synthetic and biological systems.

The MAD experiment refines the atomic scattering factor, $f$, which characterizes the diffraction behavior of atoms and has a large wavelength dependence near an atom's absorption edge. More specifically, $f$ may be subdivided into 3 components: $f = f^0 + f' + if''$, where $f^0$ is the scattering factor of the unperturbed atom, and $f'$ and $f''$ are the real and imaginary components of anomalous scattering that arise as a result of X-ray absorption and therefore vary significantly near an absorption edge (13). MAD experiments are conducted by collecting many X-ray diffraction datasets at energies near the K edge of the element of interest, allowing refinement of $f'$ and $f''$ of that element while all other scattering factors remain near constant. The values of $f''$ are only reliable for noncentrosymmetric crystals, so while recent protein crystallography examples of MAD utilize both $f'$ and $f''$, MAD analysis of synthetic polynuclear clusters is typically limited to $f'$ (14). While $f''$ is linearly related to the absorbance and therefore can be analyzed similarly to an X-ray absorption spectroscopy (XAS) spectrum, $f'$ is related to $f''$ by a Kramers–Kronig transformation and is more sensitive to fine features of the absorption edge (14).

MAD has been utilized extensively in polycrystalline systems (14–18) but only scarcely in single-crystal experiments (19–26). Given the dearth of literature surrounding single-molecule, single-crystal MAD applications, we were interested in applying the methodology to a family of well-defined clusters to examine how well this technique can resolve differences in atomic scattering factors and what molecular features affect the scattering factors themselves. Additionally, we sought to utilize this set of sample molecules to examine the interpretation of well-resolved experimental $f'$ curves. Toward this end, we selectively examined synthetic iron complexes so that comparisons could be made between the MAD results and analysis of local bond metrics and $^{57}$Fe Mössbauer parameters.

## Results

**Synthesis.** To test the applicability of MAD toward identifying the individual metal electronic environments within a cluster, we generated a family of trinuclear clusters that allowed us to probe the effects of cluster symmetry, local metal ion primary coordination sphere, M–M bonding, and cluster oxidation state changes. The asymmetric, all-ferrous complex ($^{tbs}$L)Fe$_3$(py) (**1**) allows us to examine how major differences within the cluster ions' primary coordination spheres might affect the $f'$ curves. Complex **1** can be rapidly converted to the $C_3$-symmetric chloride [$^n$Bu$_4$N][($^{tbs}$L)Fe$_3$($\mu^3$–Cl)] (**2**) adduct by treatment with [$^n$Bu$_4$N]Cl in tetrahydrofuran (THF) (Fig. 1). The symmetry of **2** is apparent in solution by the $C_3$-symmetric $^1$H NMR spectrum. The neutral phenylimido complex ($^{tbs}$L)Fe$_3$($\mu^3$–NPh) (27) (**3**) was selected as a representative mixed-valence complex, and thus we targeted its all-ferrous congener through chemical reduction. The dianionic imido was obtained via treatment of **3** with 2 equivalents of KC$_8$ in thawing THF followed by encapsulation of the K cations with [2.2.2]cryptand (C$_{222}$) to afford [K(C$_{222}$)]$_2$[($^{tbs}$L)Fe$_3$($\mu^3$–NPh)] (**4**).

**Solid-State Molecular Structures.** The solid-state structures for complexes **1**–**4** (Fig. 2) were obtained at 100 K and at an incident X-ray energy of 30.5 keV, well beyond the iron K edge. The solid-state structure for **1** retains the asymmetric binding of the $^{tbs}$L$^{6-}$ ligand about the trinuclear core reported for its THF-bound congener ($^{tbs}$L)Fe$_3$(thf) (28). As in ($^{tbs}$L)Fe$_3$(thf), **1** contains one 4-coordinate entirely ligand-bound site [Fe1–N$_{avg}$ 2.061(3) Å], one 4-coordinate solvent-bound site [Fe2–N$_{avg}$ 2.118(3) Å], and one 3-coordinate site [Fe3–N$_{avg}$ 1.983(3) Å]. In addition to the differences in coordination geometry and average Fe–N distances, the Fe–Fe distances of **1** are also distinct: Fe1–Fe2 2.6499(7), Fe1–Fe3 2.6306(7), Fe2–Fe3 2.5422(5) Å. The solid-state molecular structure of the chloride adduct **2** is not rigorously $C_3$-symmetric, owing perhaps to crystal packing effects of the $^n$Bu$_4$N cation. Significant asymmetries are apparent in both the Fe–Cl and Fe–Fe distances (Å): Fe1–Cl, 2.5185(7); Fe2–Cl, 2.4797(6); Fe3–Cl, 2.5601(7); Fe1–Fe2, 2.8428(8); Fe1–Fe3, 2.6948(8); Fe2–Fe3, 2.8184(8). However, the average Fe–N distances of the 3 Fe sites in **2** [Fe1–N$_{avg}$ 2.028(3) Å, Fe2–N$_{avg}$ 2.027(3) Å, Fe3–N$_{avg}$ 2.023(3) Å] are indistinguishable within error. The average Fe–Fe separation of 2.7853(7) Å in **2** is expanded from **1**, indicating diminished Fe–Fe bonding overlap.

The crystallographically determined structure of phenylimido **3** was reported previously (27), although we note the following

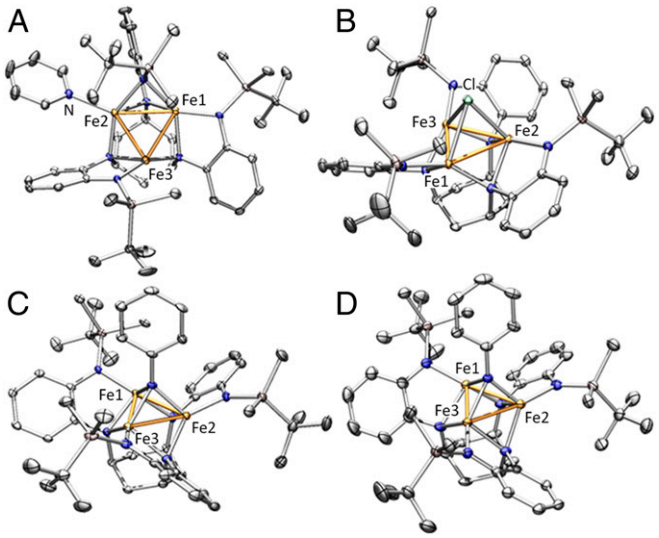


**Fig. 2.** X-ray single-crystal structures obtained at 30.5 keV (100 K) for (*A*) ($^{tbs}$L)Fe$_3$(py) (**1**), (*B*) [$^n$Bu$_4$N][($^{tbs}$L)Fe$_3$($\mu^3$–Cl)] (**2**), (*C*) ($^{tbs}$L)Fe$_3$($\mu^3$–NPh) (**3**), and (*D*) [K(C$_{222}$)]$_2$[($^{tbs}$L)Fe$_3$($\mu^3$–NPh)] (**4**). Disorder ratio of the phenyl group on the $\mu^3$–NPh fragment in **3** is 48:52. Hydrogen atoms, cations, and cocrystallized solvent molecules have been omitted for clarity. Thermal ellipsoids set at 50% probability level. Fe, orange; C, gray; Cl, green; Si, pink; and N, blue.

features: The imido phenyl moiety is found in 2 orientations in a nearly 1:1 ratio. The triiron core forms a nearly isosceles triangle, although with only a small variation in absolute distances [Fe1–Fe2, 2.5365(9); Fe1–Fe3, 2.5367(8); Fe2–Fe3 2.5133(8) Å], and the iron-imido N contacts are indistinguishable within error [Fe1–$N_{imido}$, 1.939(3); Fe2–N 1.936(4); Fe3–N 1.935(3) Å]. Lastly, there is no evidence for ligand redox noninnocence within the imido moiety [$d_{C–C\ avg}$: 1.394(20) Å] or within the $^{tbs}$L *o*-phenylenediamide units whose metrics are consistent with closed-shell dianions [$d_{C–C\ avg}$: 1.393(4) Å]. Double reduction of **3** to the dianion **4** maintains the overall aggregate geometry (Fig. 2*D*) with attendant expansion in the Fe–Fe [avg. $d_{Fe–Fe}$: 2.633(1) Å] and Fe–$N_{imido}$ [avg. $d_{Fe–NPh}$: 2.008(2) Å] interactions. The Fe–Fe distances and Fe–$N_{imido}$ distances in **4** are significantly more asymmetric than in **3**: [Fe1–Fe2, 2.6606(9); Fe1–Fe3, 2.6568(8); Fe2–Fe3 2.5817(8); Fe1–N, 1.976(2); Fe2–N, 1.991(2); Fe3–N, 2.058(2) Å].

**$^{57}$Fe Mössbauer.** The reported zero-field, $^{57}$Fe Mössbauer spectrum for **1** (Fig. 3*E*) indicates 3 unique iron environments that can be assigned to the 3-coordinate site (δ, $|\Delta E_Q|$ (mm/s): 0.33, *1.84*, blue trace); 4-coordinate, tetraanilido-bound site (δ, $|\Delta E_Q|$ (mm/s): 0.55, *1.76*, green trace); and the 4-coordinate, pyridine-bound site (δ, $|\Delta E_Q|$ (mm/s): 0.74, *1.39*, yellow trace), respectively. For **2**, the solid-state $^{57}$Fe Mössbauer displays a single quadrupole doublet [δ, $|\Delta E_Q|$ (mm/s): 0.72, *1.31*, Fig. 3*D*], consistent with the $C_3$-symmetric $^1$H NMR spectrum, but relatively surprising given the degree of asymmetry in Fe–Fe and Fe–Cl distances observed by single-crystal X-ray diffraction studies (Fig. 2*B*). The single quadrupole doublet observed for **2** also contrasts with the $^{57}$Fe Mössbauer spectrum of **4**, which has 2 distinct signals in a 1:2 ratio [δ, $|\Delta E_Q|$ (mm/s), %: 0.72, *1.47*, 35%, blue trace; 0.75, *2.84*, 65%, Fig. 3*F*]. The asymmetry of **4** by Mössbauer decreases upon oxidation, as seen in the Mössbauer spectrum of **3**, which was best modeled as 3 closely overlapping quadrupole doublets with the following parameters [δ, $|\Delta E_Q|$ ($^{mm}/_s$)]: 0.40, *1.08*, (blue trace); 0.37, *1.72*, (yellow trace); and 0.41, *2.13*, (green trace) as shown in *SI Appendix*, Fig. S12.

**Assessing the Mixed-Valent Character of ($^{tbs}$L)$Fe_3$($\mu^3$–NPh) (3).** The electrochemical behavior of **3** displays three 1-electron redox events in THF, 2 reversible reductions at $E_{1/2} = -1.25$ and $-2.48$ V, and 1 quasireversible oxidation at $E_{pa} = -0.12$ V vs. $[Cp_2Fe]^{0/+}$ (27). From these data, the upper limit for the comproportionation constant ($K_c$) (29) of **3** was calculated to be $1.3 \times 10^{19}$ (the $E_{1/2}$ of the first reduction and the $E_{pa}$ of the oxidation event were used), well in excess of $10^6$ to $10^7$ typically observed for fully delocalized mixed-valent species (Robin–Day designation of Class III) (30, 31). While the conditions used in the electrochemical experiment can vary $K_c$ (32), the latter value vastly exceeds the threshold for strongly delocalized complexes. Complex **3** was probed by zero-field $^{57}$Fe Mössbauer spectroscopy, as described above, where strongly delocalized mixed-valent systems appear as a single quadrupole doublet (33). The isomer shift values (δ), reflective of the relative oxidation levels, vary minimally among the modeled components. The variation observed for the quadrupole splitting values ($|\Delta E_Q|$) could reflect an electronic asymmetry induced by the $\mu^3$–NPh fragment,

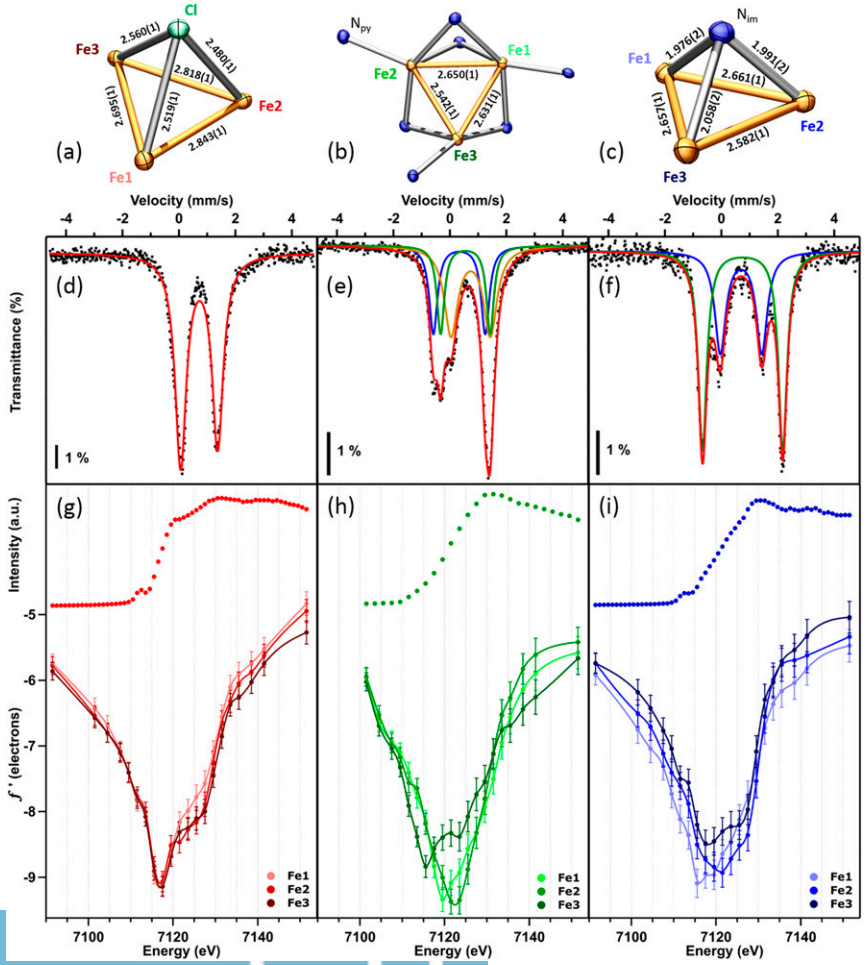


**Fig. 3.** Crystal-structure cores with bond metrics indicated and zero-field $^{57}$Fe Mössbauer spectra of the all-ferrous materials (*A* and *D*) [($^{tbs}$L)$Fe_3$($\mu^3$–Cl)]$^-$ (**2**), (*B* and *E*) ($^{tbs}$L)$Fe_3$(py) (**1**), and (*C* and *F*) [($^{tbs}$L)$Fe_3$($\mu^3$–NPh)]$^{2-}$ of (**4**). (*G–I*) Single-crystal X-ray fluorescence scan collected around the Fe K edge in steps of 1 eV at 100 K; anomalous scattering factor *f′* (filled circles) and interpolation (solid line) for each iron center of (*G*) [($^{tbs}$L)$Fe_3$($\mu^3$–Cl)]$^-$ (**2**), (*H*) ($^{tbs}$L)$Fe_3$(py) (**1**), and (*I*) [($^{tbs}$L)$Fe_3$($\mu^3$–NPh)]$^{2-}$ (**4**).

or simply result from the different orientations of the imide phenyl unit in the solid-state measurement. However, the phenomenon appears to be electronic in nature as 3 distinct components were resolved in spectra collected in an amorphous glass (toluene, 90 K, *SI Appendix*, Fig. S13) and as a polycrystalline solid at 90, 150, and 210 K (*SI Appendix*, Fig. S12).

The absorption spectrum of **3** in $C_6D_6$ displays a discernible weak absorption band at ~4,500 $cm^{-1}$; however, upon investigating the near-IR spectrum of dianionic homovalent analog **4** we observed a band of a similar intensity, shape, and energy (*SI Appendix*, Fig. S15), leading us to conclude that this feature does not arise from intervalence charge transfer in **3**. The NIR region of the absorbance spectrum of **3** is otherwise featureless. A previously reported well-characterized, strongly delocalized Class III reduced triiron complex on the same ligand platform also displayed no observable intervalence charge transfer (IVCT) band, which supports the conclusion that mixed valency in **3** is also strongly delocalized (34).

**Multiwavelength Anomalous Diffraction.** Application of MAD to the series of all-ferrous clusters **1**, **2**, and **4** consisted of collecting 37 partial diffraction datasets around the experimentally determined Fe K edge, in addition to a full data structure collection at high energy as a reference (30.5 keV). A fluorescence scan on a crystalline sample of ferrocene was used as an energy reference standard between data collections. Before collecting the diffraction data, fluorescence data were obtained on the same single crystal at steps of 1 eV from 7,080 to 7,180 eV. A highlighted region from 7,100 to 7,140 eV is shown for **2**, **1**, and **4** in Fig. 3 *D*–*F*, respectively, and for **3** in Fig. 4. No attempt was taken to determine the edge from these data and instead it was used to define the number and size of energy steps at which to collect diffraction data for the MAD experiment. For the more symmetric complexes **2**–**4**, a preedge feature is apparent between 7,110 and 7,115 eV (35, 36).

Partial diffraction data, consisting of 500 to 1,000 unique reflections at each energy, were collected around the Fe K edge in between 7,085 and 7,150 eV. When refining the partial diffraction datasets only the real ($f'$) and imaginary ($f''$) scattering factors for each iron site were freely refined while position and occupancy of all atoms were held constant from the full structures determined at 30.5 keV. Tabulated scattering factors at each energy were used for non-Fe atoms. The $f'$ plots for each iron site obtained from the refinement using the 30.5-keV reference are shown in Fig. 3 *G*–*I* for **2**, **1**, and **4**, respectively, and in Fig. 4 for **3**. The site labeling corresponds to the atomic positions shown in Fig. 1.

In a previous study of a mixed-valent $Fe^{II}Fe^{III}_2$ oxo-bridged trimer (21) a clear distinction of the minimum of the $f'$ vs. energy curves, which indicates the edge position, allowed an unambiguous assignment of the relative oxidation states of the individual metal sites. For iron-containing species, benchmark studies provide baseline energy values of $Fe^0$ (7,113 eV), $Fe^{II}$ (7,121 eV), and $Fe^{III}$ (7,127 eV), giving a narrow energy breadth spanning only 14 eV (21). The asymmetry within each $f'$ curve is likely due to the surveying of different transitions at low energy (i.e., preedge and rising-edge absorptions) compared with those surveyed at high energy (i.e., white-line energy). Initial inspection of the $f'$ curves for the asymmetric py-adduct **1** reveals a complex series of plots that span a broad range of energies, unlike those previously reported for molecular systems (21). However, the breadth of the curves is similar to those reported for polynuclear iron metalloproteins (22, 25). Remarkably, the 3-coordinate site Fe3 presents the lowest energy minimum at 7,115.5 eV, offset from the minima displayed by the 4-coordinate, tetraanilido-bound Fe1 (7,119.5 eV) and the 4-coordinate, py-bound Fe2 (7,125.5 eV). The data for [$^n$Bu$_4$N][($^{tbs}$L)Fe$_3$($\mu^3$–Cl)] (**2**) (Fig. 3 *A*, *D*, and *G*) reveal essentially overlapping $f'$ curves for all 3 iron sites. Each of the iron site traces project a sharp minimum at 7,117.5 eV; however, the energy of this minimum is coincident with a strong, in-edge absorption in the fluorescence

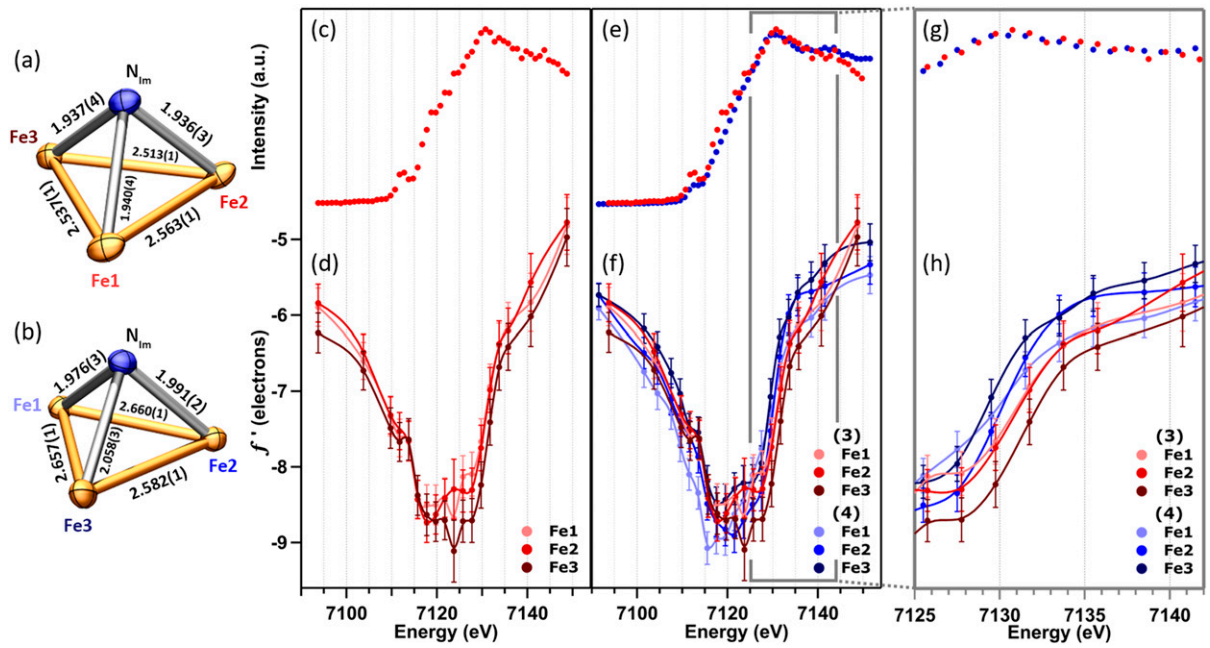


**Fig. 4.** Crystal-structure cores for ($^{tbs}$L)Fe$_3$($\mu^3$–NPh) (**3**) (*A*) and [($^{tbs}$L)Fe$_3$($\mu^3$–NPh)]$^{2-}$ of **4** (*B*) with relevant bond metrics indicated. (*C*) Single-crystal X-ray fluorescence scan collected around the Fe K edge in steps of 1 eV at 100 K and (*D*) anomalous scattering factor $f'$ (filled circles) and interpolation (solid line) for each iron center of ($^{tbs}$L)Fe$_3$($\mu^3$–NPh) (**3**). (*E*) X-ray fluorescence scan overlay for ($^{tbs}$L)Fe$_3$($\mu^3$–NPh) (**3**, red) and [($^{tbs}$L)Fe$_3$($\mu^3$–NPh)]$^{2-}$ (**4**, blue). (*F*) Overlay of anomalous scattering factor plots for each iron center of ($^{tbs}$L)Fe$_3$($\mu^3$–NPh) (**3**, red) and [($^{tbs}$L)Fe$_3$($\mu^3$–NPh)]$^{2-}$ (**4**, blue). Expanded view of the right-hand side of (*G*) the X-ray fluorescence and (*H*) $f'$ of **3** and **4** highlighting the observed shift.

scan. This feature has been observed in other chloride-containing transition-metal complexes (37). Aside from this in-edge feature, the $f'$ curves for **2** are similarly broad to those of **1**.

Examination of the scattering factors of the dianionic imido **4** reveals that each of the 3 iron sites feature significantly broadened energy minima envelopes spanning 6 to 12 eV [absolute minima (eV): Fe1, 7,115.5; Fe2, 7,121.5; Fe3, 7,117.5]. The asymmetry between the individual envelopes could be influenced by the asymmetry in the individual Fe–$N_{imido}$ distances, but further interpretation is precluded by the minimal statistical significance of the site-to-site differences in $f'$.

Application of the MAD protocol to the mixed valent ($^{tbs}$L)$Fe_3(\mu^3$–NPh) **3** reveals an analogously broad scattering factor envelope (Fig. 4*E*) akin to that observed in **4**. The nominal 2-electron oxidation on going from **4** to **3** is manifest in a subtle shift of the right side of the envelope of **3** to higher energies than in **4**. The shift in aggregate oxidation levels is more evident in comparison with the scattering factor envelopes than the composite fluorescence scans which are overlaid for **3** and **4** in Fig. 4*C*.

## Discussion

The MAD data collection strategy implemented in this study resulted in high-resolution $f'$ data for the complexes of interest. We were able to both collect energy data points at a separation of as little as 2 eV and collect sufficient data to minimize error in $f'$ such that 3 sites within a similar ligand environment can be distinguished. The resulting $f'$ curves for all-ferrous **1**, **2**, and **4**, and mixed-valent **3** allowed us to discern the effects of molecular symmetry, changes in the primary coordination spheres for the metals within the cluster, the nature of the cluster capping ligand, and cluster oxidation state. Several general observations were apparent upon comparison of our data to that for previously reported complexes. First, the $f'$ envelopes observed for the clusters examined in this study span a broader range than previously observed in molecular systems; this broadness is also observed in the fluorescence scans, and by comparison with the XAS literature (38) indicates a much higher degree of covalency within our clusters. Additionally, at the data resolution used in this study (limited by the 1-eV energy uncertainty of the synchrotron beamline at which these data were collected), observing and interpreting preedge features via $f'$ is challenging.

Probing the effect of coordination environment via MAD, the $f'$ plots of **1** reveal a strong correlation between changes in individual primary coordination spheres and the resulting anomalous scattering factors. Compared with the broad and entirely featureless fluorescence scan, the individual $f'$ curves for **1** can resolve detailed features of the absorbance at each site, including multiple transitions in the edge of the 3-coordinate site Fe3. This highlights the importance of employing a site-resolved technique for cluster complexes, as none of these features are apparent in the bulk measurement. Despite consisting of 3 formally $Fe^{II}$ sites, the disparity in the $f'$ minima span 10 eV (which nearly spans the previously benchmarked $Fe^0$–$Fe^{III}$ continuum). This case study shows that the absolute $f'$ minimum alone should not be used as an indicator of oxidation state. Rather, we note that the individual $f'$ plots converge approaching the white-line energy, suggesting the right-hand rising edge should be more reflective of the relative oxidation states of the individual sites. However, the differences in the $f'$ curves for the 3 iron sites do indicate that there is polarization across the [$Fe_3$] core, potentially signifying a disparity in local electronic structures. This analysis agrees with the $^{57}$Fe Mössbauer data for **1**, in which all 3 sites differ in both isomer shift and quadrupole splitting.

By coordinating chloride to the face of the trinuclear cluster in **2**, the local coordination environments of the individual sites are nominally symmetrized compared with those of **1**. While the M–N bonds are indistinguishable within error, the Fe–Fe and Fe–Cl distances are highly asymmetric (Fig. 3*A*), with SDs of 0.08 and 0.04 Å, respectively. Despite these differences, the $f'$ curves obtained for **2** overlay almost completely for all energies, indicating that the $f'$ plots for **2** are more reflective of Fe–N bond distances. The long Fe–Fe distances [avg. 2.785(1) Å] and Fe-Cl distances [2.519(1) Å], coincident $f'$ plots, and the single quadrupole doublet in $^{57}$Fe Mössbauer spectra indicate that the local electronic structure is dominated by the highly covalent Fe–N bonds. As anticipated, the in-edge feature observed in the fluorescence scan produces the strongest signal in the $f'$ curve, giving rise to the sharp minimum at 7,115.5 eV. The decreasing left-hand side of the curve includes a shoulder at 7,111.5 eV, coincident with the energy of the preedge feature in the fluorescence scan, confirming that preedge features contribute minimally to $f'$. Accounting for these detailed edge features, the overall $f'$ envelope for all 3 sites of **2** spans a similar energy range to that observed for **1**, corresponding to a similar degree of covalency between the 2 complexes.

The asymmetry in the Fe–Fe and Fe–$N_{imido}$ distances of **4** results in an asymmetric $^{57}$Fe Mössbauer spectrum. The unique quadrupole doublet (Fig. 3*F*), which significantly differs only in quadrupole splitting, could be associated with site Fe3 which bares significantly shorter average Fe–$N_{ligand}$ distances [2.043(3) Å vs. 2.070(3) Å and 2.074(3) Å] and a longer Fe–$N_{imido}$ distance [2.058(2) Å vs. 1.976(2) Å and 1.991(2) Å] compared with the remaining sites. The site-resolved $f'$ plots that arise from MAD, however, are barely distinguishable within error. The more covalent interactions between the iron sites and the $\mu^3$-capping group in **4** do not increase the breadth of the curves compared with **2**. The decreased Fe–Fe distances also do not result in significant broadening of the curves, nor do they change the energy at which the steep descent or ascent occurs. Synthetic clusters previously studied by MAD have much longer M–M distances than those found in **4** [M–M > 3 Å vs. Fe–$Fe_{avg}$ 2.633(1) Å]. The finding here that shorter Fe–Fe distances do not impact the curve width strengthens the conclusion that the breadth of peaks observed for the complexes in this study is related to metal–ligand covalency, as suggested by XANES literature. Those conducting future studies on synthetic and biological systems should note the tendency of highly covalent systems to give significantly broadened MAD signals compared with previous literature reports (21).

Upon oxidation to the neutral phenyl imido complex **3**, the cluster undergoes a significant symmetrization (SD Fe–$N_{ligand}$: 0.005 Å, Fe–$N_{imido}$: 0.002 Å, Fe–Fe: 0.013 Å vs. 0.017 Å, 0.044 Å, 0.045 Å, respectively, in **4**). Furthermore, $^{57}$Fe Mössbauer reveals a broad quadrupole doublet that can be fit as 3 closely overlapping components. Isomer shift and quadrupole splittings can be obtained from a fit to these data, but the closely overlapping nature of the doublets allows for multiple comparable fits. While the comproportionation constant and lack of IVCT band observed for **3** match well with what was observed for a fully delocalized, mixed-valent anion on the same triiron platform, the existence of multiple spectral features by $^{57}$Fe Mössbauer contrasts with the single quadrupole doublet observed in the previous example and other Class III iron complexes. In fact, closely overlapping but distinct quadrupole doublets were observed for a previous triiron system (formally $Fe^{III}{}_2Fe^{II}$) which was determined by MAD to consist of a pair of redox-delocalized sites and 1 redox-isolated $Fe^{III}$ (19, 21, 39).

Analyzing the MAD data for **3** reveals 3 coincident $f'$ traces, indicating a similar redox distribution across all 3 sites. Additionally, the $f'$ plots in **3** are more closely overlapping than those in **4**. This suggests that the dissimilarities within the $^{57}$Fe Mössbauer spectrum of **3** must arise from small differences in quadrupole splitting due to small geometric perturbations, rather than from a difference in oxidation state. MAD indicates that the 3 iron sites of **3** are identical in oxidation state. The overall 2-electron oxidation on going from **3** to **4**, however, is observable by MAD

in a 2-eV shift of the overall $f'$ envelopes to higher energies (Fig. 4*H* and *SI Appendix*, Fig. S16). The 2-eV shift in the position of the rising edge of the $f'$ curves is much greater than the barely discernible difference between the 2 fluorescence scans.

## Conclusions

The foregoing results allow the analysis of the impacts of aggregate oxidation level, changes in primary coordination sphere, and metal–metal bonding on the ability of MAD to determine site-specific redox levels. The data collection strategy employed successfully enabled the collection of up to 21 energy data points per molecule, significantly improving the resolution of the $f'$ curves obtained without sacrificing certainty in individual $f'$ values. The MAD results obtained in this study show that highly covalent systems display broad $f'$ traces, much like the broadening of XANES spectra with increasing covalency. Transitions that give rise to observable in-edge features in a simple fluorescence scan disproportionately affect $f'$ plots, whereas preedge features are difficult to discern, perhaps except at even higher resolution than was possible for this study. Differences in local coordination geometry dramatically impact the appearance of site-specific $f'$ curves. The overall $f'$ curve position is reflective of relative oxidation level in this study as seen by the shift in the $f'$ envelope when **3** is reduced to **4**. In general, the MAD results gave excellent correspondence with the $^{57}$Fe Mössbauer data, where nonoverlapping quadrupole doublets gave rise to nonsuperimposable $f'$ curves, thus portending the general utility of the technique. Furthermore, MAD was able to resolve the nature of delocalization in **3**, which was otherwise ambiguous by $^{57}$Fe Mössbauer. More broadly, these results highlight the importance of having control compounds that are as structurally similar as possible (e.g., **3** vs. **4**), as conclusions are difficult-to-impossible to draw in the absence of a direct comparison and particularly obscured by differences in geometry (**1** vs. **3**).

## Methods

Reagents, solvents, material synthetic procedures, and associated spectroscopic data are outlined in *SI Appendix*. X-ray absorption techniques are described in the text and in *SI Appendix*. MAD and crystallographic data and tables are included in *SI Appendix*.

**ACKNOWLEDGMENTS.** This work was supported by grants from the NIH (GM 098395), Department of Energy (DOE) (DE-SC0008313, DE -SC0019144), and Harvard University. R.H.S. gratefully acknowledges Consejo Nacional de Ciencia y Tecnología and Fundación México for a doctoral fellowship. C.E.J. acknowledges support from an NSF predoctoral fellowship. A.A.M. acknowledges support from Natural Sciences and Engineering Research Council of Canada Postdoctoral Fellowship. T.A.B. gratefully acknowledges support from the Dreyfus Foundation (Teacher–Scholar Award). NSF's ChemMatCARS Sector 15 is supported by the National Science Foundation under Grant NSF/CHE-1346572. This research used resources of the Advanced Photon Source, a US DOE Office of Science User Facility operated for the DOE Office of Science by Argonne National Laboratory under Contract DE-AC02- 06CH11357. Portions of this research were carried out at the Stanford Synchrotron Radiation Lightsource, a Directorate of SLAC National Accelerator Laboratory and an Office of Science User Facility operated for the US DOE Office of Science by Stanford University. The Stanford Synchrotron Radiation Lightsource Structural Molecular Biology Program is supported by the DOE Office of Biological and Environmental Research, and by the National Institutes of Health, National Institute of General Medical Sciences (including P41GM103393).

1. H. Taube, H. Myers, R. L. Rich, Observations on the mechanism of electron transfer in solution. *J. Am. Chem. Soc.* **75**, 4118 (1953).
2. H. Taube, E. S. Gould, Organic molecules as bridging groups in electron-transfer reactions. *Acc. Chem. Res.* **2**, 321 (1969).
3. H. Taube, Electron transfer between metal complexes: Retrospective. *Science* **226**, 1028–1036 (1984).
4. A. Davison, N. Edelstein, R. H. Holm, A. H. Maki, The preparation and characterization of four-coordinate complexes related by electron-transfer reactions. *Inorg. Chem.* **2**, 1227 (1963).
5. R. Eisenberg, H. B. Gray, Noninnocence in metal complexes: A dithiolene dawn. *Inorg. Chem.* **50**, 9741–9751 (2011).
6. H. B. Gray, E. Billig, The electronic structures of square-planar metal complexes. III. High-spin planar cobalt(I) and iron(I). *J. Am. Chem. Soc.* **85**, 2019 (1963).
7. H. B. Gray, R. Williams, I. Bernal, E. Billig, A spin-free square planar cobaltous complex. *J. Am. Chem. Soc.* **84**, 3596 (1962).
8. C. K. Jørgensen, Differences between the four halide ligands, and discussion remarks on trigonal-bipyramidal complexes, on oxidation states, and on diagonal elements of one-electron energy. *Coord. Chem. Rev.* **1**, 164 (1966).
9. R. Sarangi *et al.*, Sulfur K-edge X-ray absorption spectroscopy as a probe of ligand-metal bond covalency: Metal vs ligand oxidation in copper and nickel dithiolene complexes. *J. Am. Chem. Soc.* **129**, 2316–2326 (2007).
10. G. N. Schrauzer, V. Mayweg, Reaction of diphenylacetylene with nickel sulfides. *J. Am. Chem. Soc.* **84**, 3221 (1962).
11. R. K. Szilagyi *et al.*, Description of the ground state wave functions of Ni dithiolenes using sulfur K-edge X-ray absorption spectroscopy. *J. Am. Chem. Soc.* **125**, 9158–9169 (2003).
12. E. L. Muetterties, Molecular metal clusters. *Science* **196**, 839–848 (1977).
13. P. Coppens, D. Cox, E. Vlieg, I. K. Robinson, *Synchrotron Radiation Crystallography* (Academic Press, 1992).
14. M. Cianci *et al.*, Anomalous scattering in structural chemistry and biology. *Crystallogr. Rev.* **11**, 245 (2005).
15. G. H. Kwei *et al.*, Structure and valence from complementary anomalous X-ray and neutron powder diffraction. *J. Mol. Struct.* **223**, 383 (1990).
16. J. P. Attfield, Determination of valence and cation distributions by resonant powder X-ray diffraction. *Nature* **343**, 46 (1990).
17. J. P. Attfield, Resonant powder X-ray-diffraction applied to mixed-valence compounds and the possibility of site-resolved X-ray absorption-spectroscopy illustrated for $YBa_2Cu_3O_{6.27}$. *J. Phys. Chem. Solids* **52**, 1243 (1991).
18. H. Palancher, S. Bos, J. F. Berar, I. Margiolaki, J. L. Hodeau, X-ray resonant powder diffraction. *Eur. Phys. J. Spec. Top.* **208**, 275 (2012).
19. Y. Gao *et al.*, Valence contrast by synchrotron resonance scattering–Application to a mixed-valence manganese compound. *J. Am. Chem. Soc.* **114**, 9214 (1992).
20. Y. Gao, M. R. Pressprich, P. Coppens, Anomalous-scattering contrast study of the mixed-valence charge-density-wave conductor $NbSe_3$. *Acta Crystallogr. A* **49**, 216 (1993).
21. G. Wu *et al.*, Multitemperature resonance-diffraction and structural study of the mixed-valence complex $[Fe_3O(OOCC(CH_3)_3)_6(C_5H_5N)_3]$. *Inorg. Chem.* **37**, 6078–6083 (1998).
22. O. Einsle, S. L. A. Andrade, H. Dobbek, J. Meyer, D. C. Rees, Assignment of individual metal redox states in a metalloprotein by crystallographic refinement at multiple X-ray wavelengths. *J. Am. Chem. Soc.* **129**, 2210–2211 (2007).
23. W. A. Hendrickson, J. L. Smith, R. P. Phizackerley, E. A. Merritt, Crystallographic structure analysis of lamprey hemoglobin from anomalous dispersion of synchrotron radiation. *Proteins* **4**, 77–88 (1988).
24. L. Zhang *et al.*, The sixteenth iron in the nitrogenase MoFe protein. *Angew. Chem. Int. Ed. Engl.* **52**, 10529–10532 (2013).
25. T. Spatzal *et al.*, Nitrogenase FeMoco investigated by spatially resolved anomalous dispersion refinement. *Nat. Commun.* **7**, 10902 (2016).
26. R. Hernández Sánchez *et al.*, Electron cartography in clusters. *Angew. Chem. Int. Ed. Engl.* **57**, 13815–13820 (2018).
27. T. M. Powers, T. A. Betley, Testing the polynuclear hypothesis: Multielectron reduction of small molecules by triiron reaction sites. *J. Am. Chem. Soc.* **135**, 12289–12296 (2013).
28. T. M. Powers, A. R. Fout, S. L. Zheng, T. A. Betley, Oxidative group transfer to a triiron complex to form a nucleophilic $\mu^3$-nitride, $[Fe_3(\mu^3\text{-}N)]^-$. *J. Am. Chem. Soc.* **133**, 3336–3338 (2011).
29. M. D. Ward, Metal-metal interactions in binuclear complexes exhibiting mixed-valency: Molecular wires and switches. *Chem. Soc. Rev.* **24**, 121 (1995).
30. M. B. Robin, P. Day, "Mixed valence chemistry-A survey and classification" in *Advances in Inorganic Chemistry and Radiochemistry*, H. J. Emeléus, A. G. Sharpe, Eds. (Academic Press, 1968), vol. 10, pp. 247–422.
31. D. M. D'Alessandro, F. R. Keene, Current trends and future challenges in the experimental, theoretical and computational analysis of intervalence charge transfer (IVCT) transitions. *Chem. Soc. Rev.* **35**, 424–440 (2006).
32. D. M. D'Alessandro, F. R. Keene, A cautionary warning on the use of electrochemical measurements to calculate comproportionation constants for mixed-valence compounds. *Dalton Trans.*, 3950–3954 (2004).
33. R. Hernández Sánchez, S. L. Zheng, T. A. Betley, Ligand field strength mediates electron delocalization in octahedral $[(^{H}L)_2Fe_6(L')_m]^{n+}$ clusters. *J. Am. Chem. Soc.* **137**, 11126–11143 (2015).
34. R. Hernández Sánchez, A. K. Bartholomew, T. M. Powers, G. Ménard, T. A. Betley, Maximizing electron exchange in a $[Fe_3]$ cluster. *J. Am. Chem. Soc.* **138**, 2235–2243 (2016).
35. T. E. Westre *et al.*, A multiplet analysis of Fe K-edge 1s->3d pre-edge features of iron complexes. *J. Am. Chem. Soc.* **119**, 6297 (1997).
36. J. U. Rohde *et al.*, XAS characterization of a nitridoiron(IV) complex with a very short Fe-N bond. *Inorg. Chem.* **46**, 5720–5726 (2007).
37. T. Herskovitz *et al.*, Structure and properties of a synthetic analogue of bacterial iron–sulfur proteins. *Proc. Natl. Acad. Sci. U.S.A.* **69**, 2437–2441 (1972).
38. R. Sarangi, X-ray absorption near-edge spectroscopy in bioinorganic chemistry: Application to M-$O_2$ systems. *Coord. Chem. Rev.* **257**, 459–472 (2013).
39. R. W. Wu *et al.*, Electron localization and delocalization in mixed-valence transition metal clusters: Structural and spectroscopic studies of oxo-centered trinuclear complexes $[Fe_3O(OOCCMe_3)_6(py)_3)]^{+/0}$ and $[Mn_3O(OOCCMe_3)_6(py)_3]^{+/0}$. *Inorg. Chem.* **37**, 1913 (1998).